EXPERIMENTAL EVALUATION OF FLOW DISTORTION AT NGCTR OPTIMIZED AIR INTAKE FULL SCALE MODEL

Remco Habing, remco.habing@nlr.nl, Netherlands Aerospace Centre (NL)

Roy Gebbink, roy.gebbink@dnw.aero, German-Dutch Wind Tunnels (NL)

Matthias Müller, m.mueller@deharde.de, Deharde (DE)

Matteo Pecoraro, matteo.pecoraro@leonardocompany.com, Leonardo Helicopters (IT)

Gaetano Preatoni, gaetano.preatoni@leonardo.com, Leonardo Helicopters (IT)

Abstract

Within the Clean Sky 2 Fast Rotorcraft platform, a Next Generation Civil Tilt-Rotor (NGCTR) Technology Demonstrator is being developed. Within the related TRINIDAT project the key driving aerodynamic choices of the engine air intake configuration are being investigated. A wind tunnel model has been successfully designed and manufactured for full-scale intake testing of modular intake configurations. The model is comprised of a nacelle, modular intake duct, rotatable spinner hub (rotor head) and wing part including deflectable aileron. In order to assess the flow quality at the Aerodynamic Interface Plane (AIP), a novel highly instrumented rotary rake has been designed. The model also includes a large amount of static pressure taps on wing and intake duct surfaces. The results of a wind tunnel test with the basic intake configuration in the DNW-LLF have been published in an earlier paper and yield a large database containing basic intake performance and sensitivities for the full flight envelope [14]. The present paper presents the results of an optimized intake configuration which has been successfully tested in a second TRINIDAT entry at the DNW-LLF. The adopted scaling methodology is explained. The 6 x 6 m^2 test section allowed to test the full-scale model at $Ma = 0.40$ which is nearly cruise Mach number. The test program included variations in angle of attack, sideslip angle, aileron deflection and suction mass-flow rate. Post-processing of the test data yielded a large database including flow distortion parameters based on the total pressure field and the velocity field in the AIP. A comparison of key flow distortion parameters and static pressure distributions between optimized and basic intake showed that the optimized intake overall features significant improvement of the flow quality. For the aircraft mode an averaged reduction in $DC60MAX$ of 74% has been realized. The development of unsteady pressures along the optimized intake duct including AIP has been characterized as well.

1. INTRODUCTION

Within the Clean Sky 2 Fast Rotorcraft platform, a Next Generation Civil Tilt-Rotor (NGCTR) Technology Demonstrator is being developed [1] (Fig. 1). The design phase has been successfully completed [16]. The NGCTR concept is a next step in the development of a European civil tilt-rotor, following the earlier work on the AW609 programme and the ERICA concept [4]. The main benefit of the NGCTR configuration (compared to helicopter and turboprop) is that it offers reduced travel time on short and medium distances up to 500 nautical miles (approximately 1000 km). For NGCTR, to reduce system complexity and weight, it has been decided to keep the engine at fixed pitch angle setting and make only the spinner and rotor rotatable. This change of engine integration architecture requires research to assure a good flow quality in the engine intake ducts under all flying conditions, with a focus on high efficiency in aircraft mode and safe and proper operation in other flight modes.

The related TRINIDAT project [2] has two main objectives, namely i) to assess, by dedicated experiments and advanced CFD analysis, the key driving aerodynamic choices of the intakes configuration, and ii) to investigate the icing and snow effects on the intakes, providing early input for ice protection system development and certification [13]. The first objective includes a basic as well as an optimized intake duct. The present paper summarizes results of the TRINIDAT project, related to model design, test simulation methodology, test procedure and analysis results obtained from the conducted wind tunnel test with the optimized intake configuration.

Fig. 1 Artist view of NGCTR concept in cruise condition

2. WIND TUNNEL MODEL

2.1. Optimized intake duct geometry

Whereas the basic intake duct geometry is dictated by system constraints, the optimized intake duct geometry has been designed by a gradient-based optimization algorithm, where the gradient is calculated by means of the adjoint method [15]. The basic intake duct features a large flow distortion on the Aerodynamic Interface Plane (AIP) with strong flow unsteadiness [14], within engine specifications range. A cost functional measuring the deviation between an actual and a desired pressure distribution has been minimized. Due to the tilting rotor head concept of the NGCTR, the intake duct changes from an elliptical cross-section to an annular cross-section of the AIP for the engine. The optimized intake duct geometry features particular modifications in the middle sections and in front of the AIP (Fig. 2).

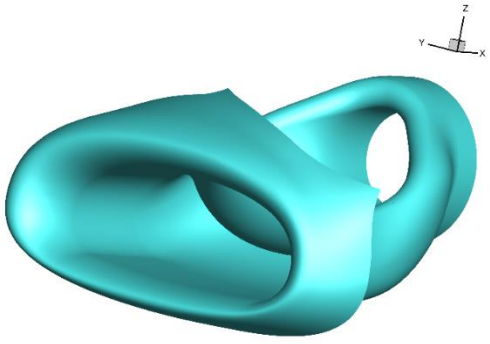

(a) basic intake

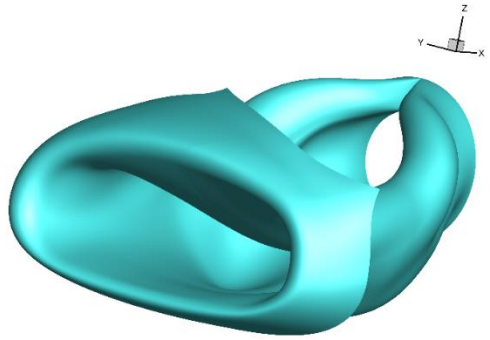

(b) optimized intake

Fig. 2 Comparison of duct geometry: basic intake (a) vs. optimized intake (b)

2.2. Model design & manufacturing

The model is comprised of a nacelle, modular intake duct, rotatable spinner hub (rotor head) and wing part including deflectable aileron (Fig. 3). The model represents a full-scale air intake excluding rotor. As for the NGCTR aircraft both rotors will rotate symmetrically, a half-model configuration is considered. The model assembly is basically comprised of three parts, i.e. nacelle, wing and wind tunnel model support. In order to be able to capture high loads an overlap of the steel wing bottom plate with the aluminium wing was realized. The wing contains cable holes and a sealed wing box with rounded suction hole. A provision for testing of vortex generators also has been realized. A trade-off between truncated wing span and allowance of sideslip settings (-10 to 10 deg) has been designed.

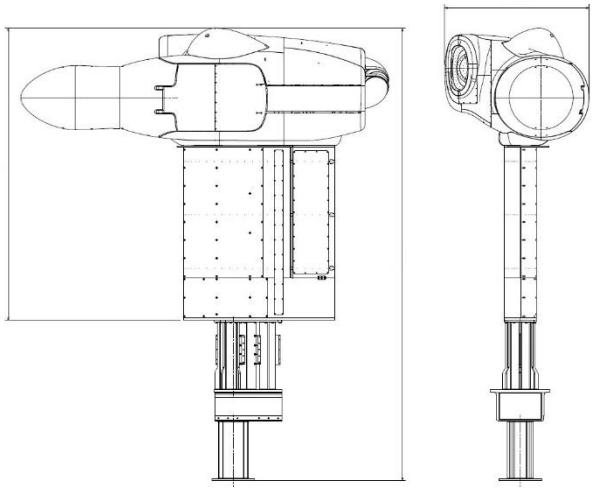

Fig. 3 Design of full-scale wind tunnel model

The optimized intake geometry has been used to design a modular wind tunnel model part (Fig. 4). In order to assess the flow quality at the AIP annulus, two key elements were addressed. First, an internal piping system is designed to allow for generating the proper suction mass flow-rate at the

AIP. Second, a specially designed rotary rake is mounted at the AIP to allow for accurately measuring the flow quality (Fig. 5). The suction pipe is designed to have sufficient axial length from AIP to first bending section to neglect the downstream flow curvature effect on the AIP.

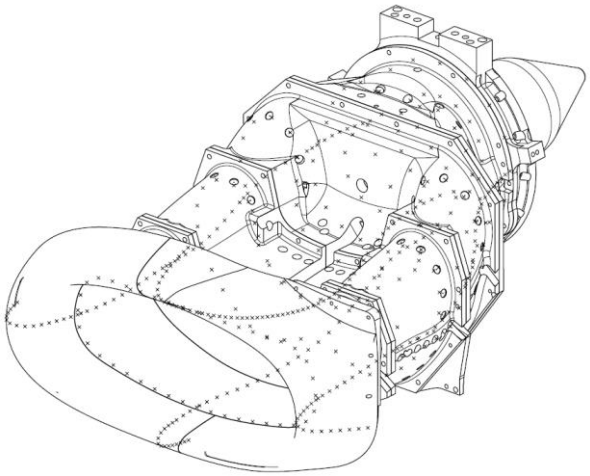

Fig. 4 Design of optimized intake model and pressure tap distribution

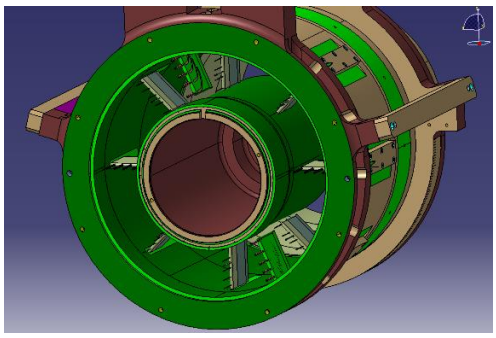

Fig. 5 Design of novel rotary rake and instrumentation at AIP

2.3. Remote controls & instrumentation

The model features three remote control systems, i.e. for aileron deflection (-30 to 70 deg, trailing edge down is positive), rotor hub pitch angle (0 to 90 deg) and rotary rake settings (-90 to 90 deg). The system drives are servo motors with adjustable gearing, flex coupling and include absolute encoders (position sensors) which have been calibrated prior to testing. The limit switches design ensures the above mentioned full range angular settings.

The highly instrumented rotary rake (Fig. 6) consists of 40 steady total pressure probes (8 equiangularly spaced rakes with 5 area-weighed radially positioned probes per rake, following SAE [3]), 10 unsteady total pressure sensors (2 dedicated rakes with co-annular design [5] for steady and unsteady total pressure), 6 total temperature sensors (integrated in pressure rakes) and 10 flow-directional probes (2 rakes, 180 deg spaced, with 5 area-weighed radially positioned 5-hole probes per rake), while keeping a very low flow blockage of 0.3% (compare e.g. Ref. [5]). The flow-directional probe rakes have been calibrated in NLR's AWT facility prior to WT testing.

The model also includes a large amount of static pressure taps (on 3 wing sections at different spanwise positions crossing the aileron (168 taps), intake lip and duct (356 taps, Fig. 4) and AIP annular surfaces (32 taps, Fig. 6)). The intake lip contains 4 streamwise tap sections, the intake duct contains 4 continued streamwise tap sections and 4 circumferential tap sections (excl. AIP). The intake duct also includes 10 flush-mounted unsteady (static) pressure sensors.

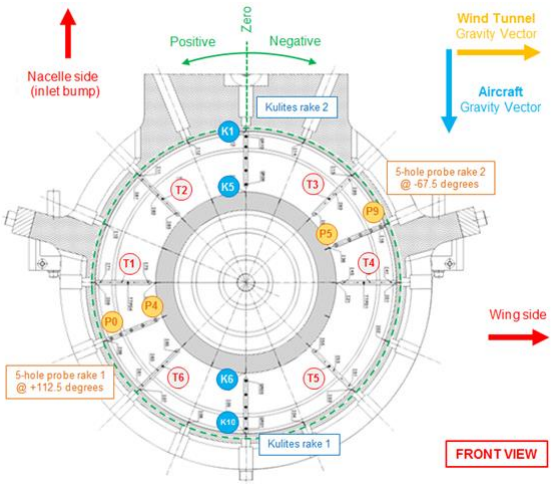

Fig. 6 Design of instrumentation layout at AIP

3. WIND TUNNEL TEST

3.1. Simulation and test conditions

Free flight conditions have been specified by Leonardo Helicopters, mainly as guidelines for the CFD simulations and covering the full flight envelope. The translation from flight- to wind tunnel test conditions is performed by application of similarity rules. The applied rules consider both the inverse capture ratio (ICR) as well as the Reynolds number (Re_{AIP}) based on bulk flow conditions at the AIP to remain constant. It can then be shown that for full-scale testing the following relation for the freestream wind tunnel velocity holds:

$$V_{WT} = \frac{\rho_{Flight}}{\rho_{WT}} \frac{\mu_{AIP,WT}}{\mu_{AIP,Flight}} V_{Flight} \quad (1)$$

Applying Sutherland's law for dynamic viscosity, this relation contains a coefficient that strongly

depends on air density and a coefficient that weakly depends on static temperature in the AIP. In general these equations need to be solved iteratively. However, it can be shown that for low Mach number in the AIP ($Ma_{AIP} < Ma < 0.4$) the static temperature in the AIP is with good approximation (≤ 3%) equal to the freestream static temperature. As iterative methods in online processing are not recommended, above approximation is employed in the translation procedure. From eq. (1) it is recognized that simulating high altitude conditions in a wind tunnel require significant reduction in wind tunnel speed (compared to free flight). It can be shown that for the Re_{AIP} similitude only a limited increase in mass flow rate is required.

As the test is performed without rotor blades, the rotor induced wind field in flight condition has been obtained from application of Glauert's rotor flow model [6]. Knowing that the rotor radius R is much larger than the air intake dimensions, it is recognized that the intake is always in the flow field generated by the rotor, for all flight modes. The rotor induced wind field v_i (i.e. rotor generated axial velocity) is obtained in an iterative procedure from the following equation:

(2) $$v_i^4 + 2Vv_i^3\cos(\theta_r + \alpha) + v_i^2V^2 = \frac{T^2}{4\rho^2\pi^2R^4}$$

where θ_r is the rotor hub pitch angle, α is the angle of attack, T is the rotor thrust. It is noted that from eq. (2) well-known limit case equations can be obtained for small induced velocities in airplane mode ($\frac{v_i}{V} \ll 1$) or significant induced velocities in hover mode ($V = 0$). With the rotor induced velocity component directed along the rotor axis, and assuming the effective total velocity magnitude and direction for the intake is the same as in the rotor plane, it is possible to derive expressions for the effective flight velocity and effective angle of attack:

(3) $$V_{e,Flight} = \sqrt{[V\cos(\theta_r + \alpha) + v_i]^2 + [V\sin(\theta_r + \alpha)]^2}$$

(4) $$\alpha_{e,Flight} = \alpha - atan\left[\frac{v_i\sin(\alpha+\theta_r)}{V+v_i\cos(\alpha+\theta_r)}\right]$$

For cruise conditions a trivial solution is obtained ($V_{e,Flight} = V$ and $\alpha_{e,Flight} = \alpha$). For hover conditions these result in $V_{e,Flight} = v_i$ and $\alpha_{e,Flight} = -\theta_r$. For conversion modes these equations are of particular interest.

3.2. Test setup

The Large-Low-Speed-Facility (LLF) of DNW is an atmospheric, single return wind tunnel with three exchangeable closed test section arrangements (Fig. 7) as well as an open-jet configuration. The measurements with the TRINIDAT full-scale intake model during the second test entry were performed in the 6 x 6 m² test section (airplane mode, conversion modes and VTOL mode as well). The 6 x 6 m² test section allowed to test the full-scale model at $Ma = 0.40$ which is nearly cruise Mach number.

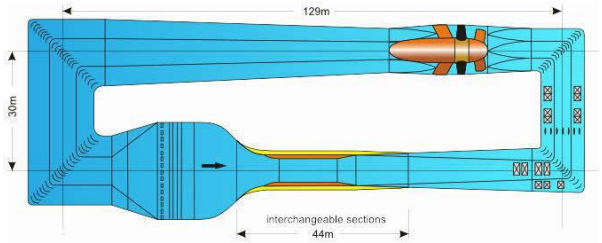

Fig. 7 Airline and dimensions of the LLF (top view)

The model is mounted on a turntable in the test section floor (which allows angle of attack variation), with direct interfacing to the alpha-mechanism (cradle) inside the turntable (allowing combined sideslip variation), see Fig. 8. The spinner hub axis at 0 deg pitch at zero angle of attack is located at tunnel centre line.

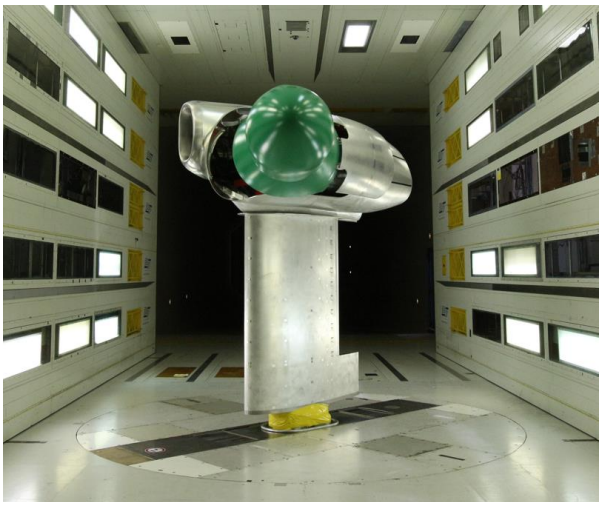
Fig. 8 Full-scale model installed in DNW-LLF wind tunnel 6m × 6m test section (entry 2)

Applying homogeneous transformations yields the model geometrical setting angles from combined aerodynamic angle of attack and sideslip angle.

The model is interfaced with a suction system located underneath the test section. This system consists of a piping and measurement system with 3 Roots Blowers, which are capable to attain the maximum required mass-flow rate of 6.4 kg/s through the inlet of the intake model (test entry 2). The Roots Blowers are calibrated prior to testing.

3.3. Instrumentation & data acquisition

The standard wind tunnel reference system is calibrated prior to testing and used to obtain the freestream flow quantities. In addition six wall pressure tap strips are applied on the test section walls to allow for blockage correction evaluations. The model instrumentation includes measurement of model incidence and roll angle, steady pressures, unsteady pressures, temperatures and position of the remote controls.

All data is acquired in step and pause mode. In order to meet the SAE requirements [3], the integration time was set to 30 s per data point (after reaching a stable test condition). The Static Data Acquisition system samples the data at a rate of 20 Hz (with LPF = 3 Hz) and stores the averaged value incl. statistics. The Dynamic Data Acquisition system is used to acquire the time signals of the unsteady pressure sensors. Following the guidelines of SAE [3], taking into account sources of unsteadiness such as freestream turbulence and possible flow separation at intake duct, a sampling rate of 12.8 kHz during 30 s is used.

3.4. Test program & procedure

The test program includes full flight conditions, high-speed conditions and parameter variations (angle of attack, sideslip, aileron deflection, mass-flow rate) for airplane mode (AP), conversion modes (CM, rotor hub pitch 30, 50, 75 deg) and VTOL mode. The conducted test matrix included a wide variety of model attitude (i.e. rotor hub pitch [0, 90], effective angle of attack [-90, 37], sideslip [-10, 10], aileron [-30, 70], all in deg).

The following procedure was applied for setting the test flow conditions. The test matrix contained estimations of the required mass-flow rate and freestream velocity, based on the adapted scaling methodology (see 3.1). First, the required Reynolds number was set by control of the mass-flow rate W_{WT}, see eq. (5). Then the inverse capture ratio was set by control of the freestream velocity V_{WT} subsequently, see eq. (6).

(5) $$Re_{AIP} = \frac{(W_{WT}/A_{AIP})}{\mu_{WT}} D_{h,AIP}$$

(6) $$ICR = \frac{\rho_{WT} V_{WT}}{(W_{WT}/A_{AIP})}$$

These scaling parameters have following required values for the full flight conditions: $3.4\text{E}5 \leq Re_{AIP} \leq 6.7\text{E}5$ and $0.3 \leq ICR \leq 1.8$.

The spatial resolution of the flow measurements in the AIP has been increased by using the rotary rake. The test matrix contained 4 types of settings, i.e.

- [0] deg, fixed rake, mean Pt field
- [45, 67.5, 90] deg, rotating rake, refined mean Pt field (and swirl in top/bottom sector)
- [45 (7.5) 90] deg, rotating rake, extra refined mean Pt field (and swirl in top/bottom sector)
- [-90 (15) 75] deg, rotating rake, full scan for complete flow field (incl. swirl and unsteady pressure)

Following the SAE regulations [3], in clockwise direction is considered positive for pilot view (i.e. upstream looking), see also Fig. 6.

Considering all test conditions, the static temperature in the AIP deviates on average 0.5% (and no more than 2.1%) from the freestream static temperature. This confirms an important assumption of the scaling methodology (3.1).

3.5. Data processing

The data processing system allows online and offline data processing, presentation and storage of measured data. A dedicated tool for online checking the intake- and wing performance has been developed during test entry 1, see Fig. 9. The final results are corrected for zero drift of the instrumentation and blockage of the wind tunnel model.

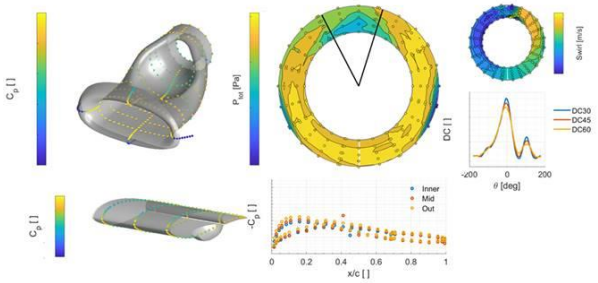

Fig. 9 Dedicated online monitoring tool

During the test entry 1 execution online blockage correction was performed with the neo-classical corrections [8,9]. As the wind tunnel model is not

equipped with a force balance, only corrections for solid blockage (wing, nacelle) and inlet blockage are considered. The final test entry 1 data was established by replacing the neo-classical corrections by an offline blockage correction based on a wall pressure signature method [10,11]. The wind tunnel test entry 2 has been performed with an online blockage correction using the wall pressure method. The final data has thus been corrected for wall induced flow blockage effects, which can be considerable for large angle of attack (for AP mode a typical value of 6% is found, while for VTOL mode typically 22% is found).

Finally, it is stated that during test entry 1 the basic intake has been investigated, while for entry 2 both the optimized intake and the basic intake have been tested. The back-to-back testing of both intakes within entry 2 allowed for direct comparison of the AIP flow distortion parameters at full flight conditions (as shown in the remaining part of the present paper), as well as for a repeatability comparison with entry 1.

4. ANALYSIS OF TEST DATA

4.1. Flow distortion parameters

The importance of the effect of flow non-uniformities on an aeroengine has resulted in the development of a range of reduced-order parameters to quantify the level of distortion being presented to the engine [3,7]. The flow quality at the AIP of the basic intake model has been characterized by calculation of flow distortion parameters in dedicated MATLAB® scripts, taking the final test data as input. These parameters are largely based on the distribution of total pressure in the AIP.

The total pressure distortion at the AIP is quantified in terms of sectional distortion coefficient $DC60(\theta)$, circumferential distortion index CDI and radial distortion index RDI. $DC60(\theta)$ is defined by the difference between the area-averaged total pressure at the AIP $\overline{p0_{AIP}}$ and the average total pressure in a sector of 60 deg at circumferential mid-angle $\overline{p0_\theta}$ and is non-dimensionalized by the mean dynamic head of the whole AIP $\overline{q_{AIP}}$ as

$$(7) \qquad \mathrm{DC60}(\theta) = \frac{\overline{p0_{AIP}} - \overline{p0_\theta}}{\overline{q_{AIP}}}$$

At the maximum of the profile, two parameters are defined; $DC60MAX$ as maximum value and θ_{max} as related angular position. The CDI assesses the uniformity of the circumferential total pressure distribution at a specific radial position and is defined as

$$(8) \quad \mathrm{CDI} = max_{i=1}^{4}\left(\frac{1}{2}\left[\frac{\overline{p0_i} - \min(p0)_i}{\overline{p0_{AIP}}} + \frac{\overline{p0_{i+1}} - \min(p0)_{i+1}}{\overline{p0_{AIP}}}\right]\right)$$

where $\overline{p0_i}$ is the average total pressure of the circumferential pressure distribution of the i^{th} ring (i=1..5) and $\min(p0)_i$ is the minimum total pressure along this same ring. Non-uniformities in the radial distortion are evaluated by the RDI which is defined as

$$(9) \qquad \mathrm{RDI} = max\left(\frac{\overline{p0_{AIP}} - \overline{p0}_{i=1}}{\overline{p0_{AIP}}}, \frac{\overline{p0_{AIP}} - \overline{p0}_{i=5}}{\overline{p0_{AIP}}}\right)$$

where $\overline{p0}_{i=1}$ is the average total pressure of the pressure distribution of the inner ring and $\overline{p0}_{i=5}$ is the average total pressure at the outer ring.

Additional metrics have been developed that consider total pressure distortion as a ring-based radial distribution of specific parameters, where radial and circumferential distortions are quantified separately. The circumferential total pressure distribution $p0$ is considered in terms of an average $\overline{p0_i}$ and regions of low relative total pressure ($p0 < \overline{p0_i}$) and high relative total pressure ($p0 > \overline{p0_i}$). The extent parameter for a one-per-revolution pattern is defined as the circumferential extension of the low-pressure region [3], i.e. $\theta_i^- = \theta 2_i - \theta 1_i$. The circumferential distortion intensity for ring i is defined as:

$$(10) \qquad (\Delta P_C/P)_i = \left(\frac{\overline{p0_i} - \overline{p0_-}}{\overline{p0_i}}\right)_i$$

where

$$(11) \qquad \left(\overline{p0_-}\right)_i = \frac{1}{\theta_i^-}\int_{\theta 1_i}^{\theta 2_i} p0(\theta)_i \,\mathrm{d}\theta$$

The radial distortion intensity is calculated from the difference between the average total pressure of ring i and the average of the whole AIP:

$$(12) \qquad (\Delta P_R/P)_i = \frac{\overline{p0_{AIP}} - \overline{p0_i}}{\overline{p0_{AIP}}}$$

The total pressure recovery at the AIP is defined as an overall performance parameter:

$$(13) \qquad C_{dh} = \frac{\rho_{inf}\left(p0_{inf} - \overline{p0_{AIP}}\right)}{W^2}$$

where ρ_{inf} is the freestream density, $p0_{inf}$ is the freestream total pressure and W is the intake mass-flow rate.

In addition to total pressure based parameters, some used parameters are based on the velocity

field in the AIP. The distortion descriptor applied for swirl-based non-uniformities is considered in terms of the $SC60(\theta)$ parameter. It is defined as the ratio of $\overline{|V_{\theta 60}|}$, the average value of the absolute circumferential velocity in a section of 60 deg (from a rotating rake), to the mean axial velocity $\overline{u_{AIP}}$:

$$SC60(\theta) = \frac{\overline{|V_{\theta 60}|}}{\overline{u_{AIP}}} \quad (14)$$

The maximum value of the profile is defined as $SC60MAX$ and its related angle θ_{SCmax}. The swirl angle Φ is defined as the circumferential angle from the axial direction of the velocity vector and is considered positive in the clockwise direction looking at the AIP from downstream (i.e. pilot view):

$$\Phi = \tan^{-1}\left(\frac{U_\theta}{U_x}\right) \quad (15)$$

It is noted that the velocity field in the AIP is obtained from the rotating flow directional probes test data by application of the calibration coefficients and several post-processing steps [12].

In order to investigate possible flow separation effects, the steady and unsteady static pressure distribution along the intake- lip and duct surfaces have also been obtained.

4.2. Full flight conditions

The tested full flight conditions are comprised of various aircraft speed, pressure altitude, angle of attack, sideslip angle, ambient temperature, rotor hub pitch, engine mass-flow rate and one rotor thrust settings, being representative for the full flight envelope.

The present paper only considers experimental results comparisons between basic and optimized intake configurations for full flight conditions. Similar comparison analysis has been performed for the $DC60MAX$ predictions made by CFD simulations [15]. Fig. 10 illustrates all prescribed flight conditions (load cases), where conditions 8 and 12 have not been considered during the second test entry (due to sideslip range limitations and test program reduction, resp.).

LC	1	2	3	4	5	6	7	8
Mode	Airplane							
LC	9	10	11	12	13	14	15	
Mode	Conversion			VTOL				

Fig. 10 Overview of TRINIDAT load cases

4.3. Flow quality at AIP comparison

Fig. 11 shows an example of the distribution of the total pressure in the AIP. The contour plots depict the angular position (SAE convention) and AIP annulus walls. The total pressure is made dimensionless by normalizing against the free-stream total pressure. This eases comparison between intake configurations, different test conditions and allows interpretation of the total pressure loss. In general, it can be observed that the top sector shows two local areas with relatively low total pressure values. The optimized intake shows i) a splitter plate (see Fig. 2) wake effect at 0 deg in addition, ii) more localized low total pressure zones with higher levels.

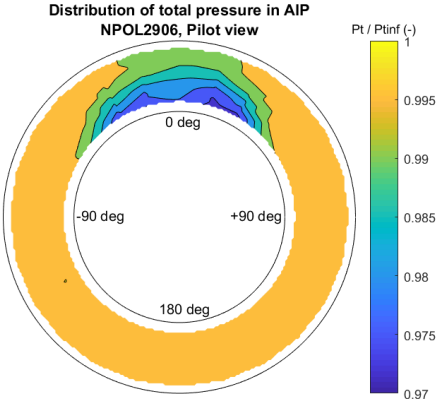

(a) basic

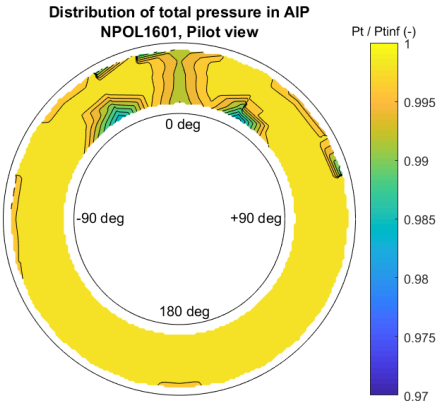

(b) optimized

Fig. 11 Comparison of total pressure distribution in AIP for an AP mode condition

Fig. 12 shows an example of the distribution of the swirl angle in the AIP. In general, it can be observed that the top sector shows two local areas with relatively high circulation. The flow particles move circumferentially at radial outward located streamlines towards approx. 0 deg and then move at radial inward located streamlines from the approx. 0 deg plane away. It can be observed that the swirl angle distribution is not always perfectly

anti-symmetric (referred to the approx. 0 deg plane), however, the optimized duct appears to enhance the anti-symmetry in the velocity field pattern.

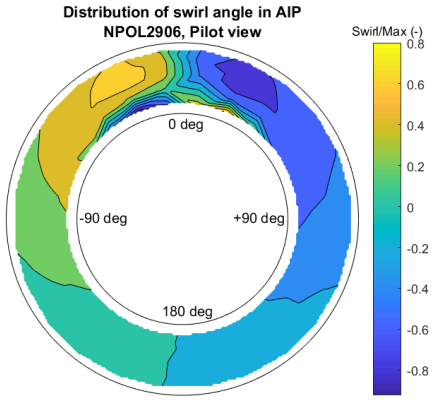

(a) basic

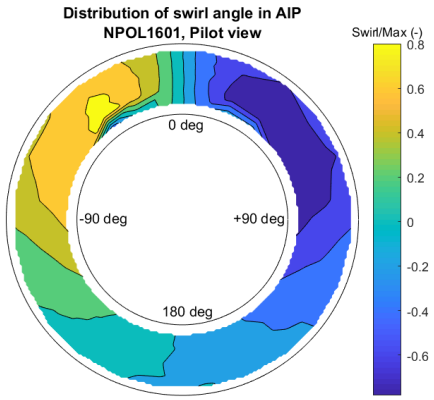

(b) optimized

Fig. 12 Comparison of swirl angle distribution in AIP for an AP mode condition

Prior to generation of a database with distortion parameters $DC60(\theta)$ and $SC60(\theta)$, it has to be decided which value the sector scanning resolution should have. Analysis showed that a converged solution can be obtained if the sector scanning resolution is smaller than the step size of the rotating rake. It was decided to set the scanning resolution equal to 1 deg (the lowest used step size for the rotating rake is 7.5 deg). This results in plots with a typical staircase profile.

Fig. 13 shows an example of $DC60(\theta)$ and Fig. 14 of $SC60(\theta)$. In order to allow quantitative statements about the flow quality improvement of the optimized intake (without releasing absolute values), the plots have been non-dimensionalized with the maximum value of the basic intake profile. In general, it can be observed that the total pressure distortion $DC60(\theta)$ has a single maximum at the top sector of the AIP. The optimized intake shows a significantly lower and broadened maximum. For the swirl distortion $SC60(\theta)$, however, two local maxima exist, in which the maximum is generally found at another angle than for $DC60(\theta)$. This is related to the area weighing factor being larger for radially outward flow topologies, in combination with a slightly asymmetric absolute velocity field. The optimized intake appears to enhance the localization of the peaks (and slightly the symmetry) of the $SC60(\theta)$ profile, without significantly reducing its maximum value.

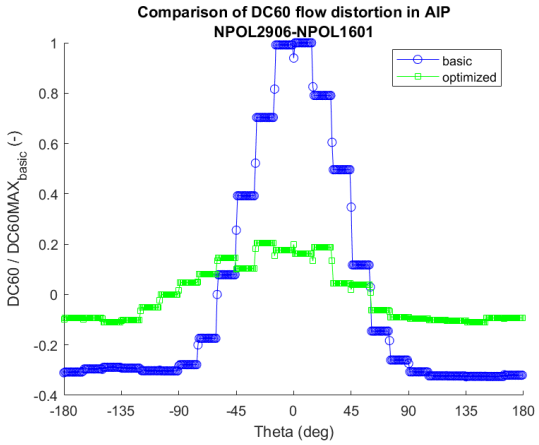

Fig. 13 Comparison of DC60 profile for an AP mode condition

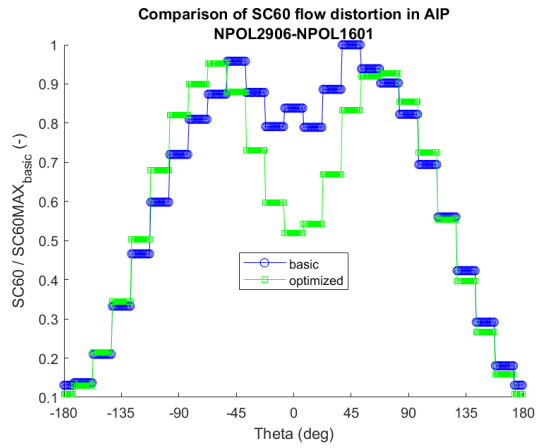

Fig. 14 Comparison of SC60 profile for an AP mode condition

The $DC60MAX$ parameter allows for a first evaluation of the intake flow quality for the set of full flight conditions. For the basic intake it was found from test entry 1 that only minor differences exist in the averaged value for the AP mode, CM and VTOL subsets [14]. Fig. 15 shows the non-dimensionalized $DC60MAX$ bar chart for basic- and optimized intake for all tested flight conditions of test entry 2. It can be observed that significant reduction is obtained with the optimized intake duct for all conditions. For AP and CM mode the

averaged reduction is 74% and for VTOL mode 59% is obtained. Analysis of the distortion indices showed that the circumferential index CDI is in general much larger than the radial index RDI, for basic- and optimized intake. A reduction of CDI with the optimized intake is found for all conditions. Similar trends are found for the radial distortion intensity $(\Delta P_R/P)_{max}$ and circumferential distortion intensity $(\Delta P_C/P)_{max}$.

Fig. 16 shows the non-dimensionalized $SC60MAX$ bar chart for basic- and optimized intake for all tested flight conditions of test entry 2. As also found for test entry 1 [14], it can be observed that the largest values for the basic intake are found for the AP mode. The optimized intake shows minor reduction for all conditions (i.e. 9% for AP, 4% for CM and 3% for VTOL), where the largest values changes to VTOL modes.

Fig. 17 shows a comparison of the intake performance, i.e. the non-dimensionalized C_{dh} bar chart for basic- and optimized intake for all tested flight conditions of test entry 2. As also found for test entry 1 [14], it can be observed for the basic intake that the largest values of the total pressure recovery C_{dh} are found for the VTOL mode. The optimized intake shows reduction for all conditions (i.e. 50% for AP, 64% for CM and 41% for VTOL). As the distortion parameters are not showing such behaviour, additional analysis of the pressure distribution along the intake duct is required.

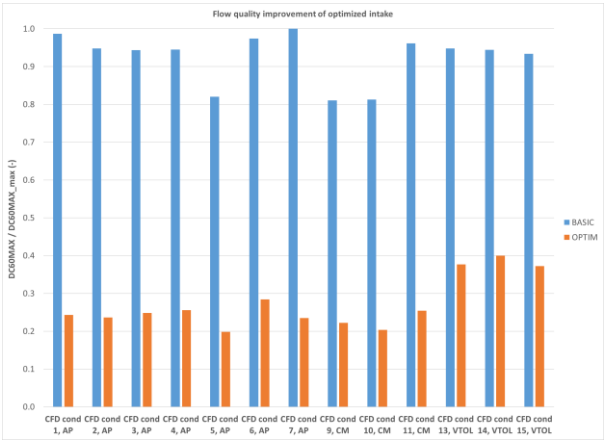

Fig. 15 Comparison of $DC60MAX$ for all considered conditions

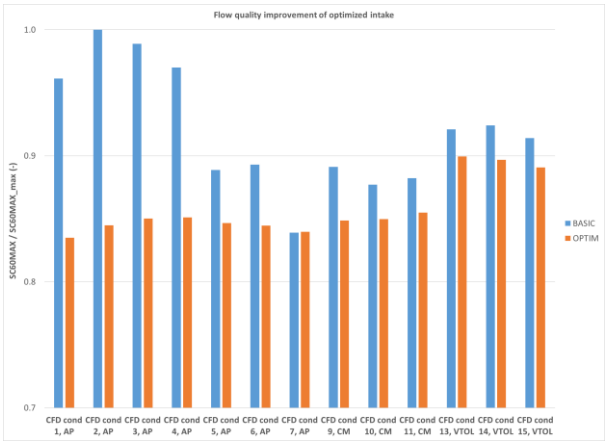

Fig. 16 Comparison of $SC60MAX$ for all considered conditions

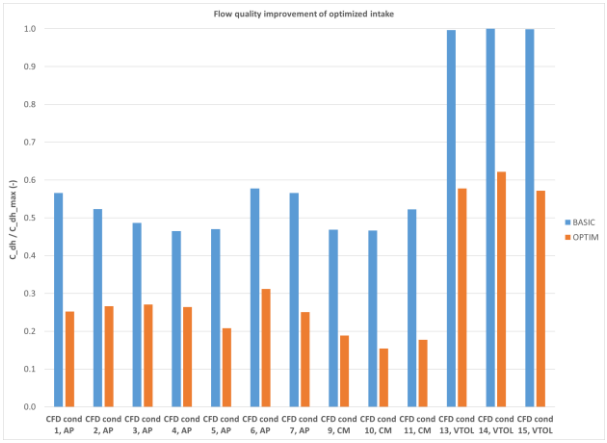

Fig. 17 Comparison of C_{dh} for all considered conditions

4.4. Pressure distribution comparison

Both the basic and optimized intake duct have a large number of static pressure taps. Based on the results of the steady and unsteady static pressure distributions of the basic intake duct [14], the optimized duct model has been designed with a deviating distribution of taps (i.e. less circumferential sections and inclusion of streamwise sections in XY-plane, see Fig. 2).

Fig. 18 shows a comparison of normalized static pressure coefficient (C_p) distributions along the intake duct (in the symmetry plane) for an AP mode. The axial development of the static pressure along the basic intake duct shows a negative gradient in front of the AIP for the top line and a positive gradient in front of the AIP for the bottom line. The positive gradient is related to a decelerating flow and in general can be considered to have a non-positive effect on the intake overall performance. The optimized intake, however, shows some different behaviour. First, the middle section (downstream of the lip) shows a flattened C_p distribution with increased levels. Second, the adverse pressure gradient along the top line in the

middle section has a reduced C_p range for the optimized intake. Third, the C_p distribution of the bottom line just in front of the AIP shows a negative slope, while the basic intake shows an adverse pressure gradient.

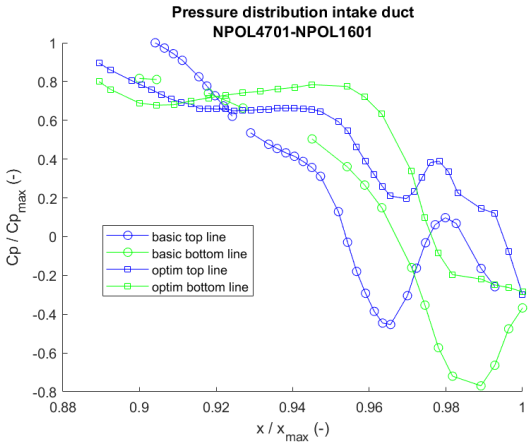

Fig. 18 Comparison of static pressure distribution intake duct for an AP mode condition

4.5. Unsteady pressure comparison

The signals of the unsteady pressure sensors appeared to contain multiple peaks in the time domain (without overloads), which complicates spectral analysis in general. In order to analyze the flow unsteadiness, RMS values are obtained from the frequency domain, in which a filter has been applied for all test conditions (i.e. HPF = 10 Hz and LPF = 500 Hz). The RMS values in the AIP have been obtained from full rotating rake polars.

Fig. 19 shows a comparison of the RMS total pressure distribution in the AIP between the basic and optimized intake for an AP mode. In general, it can be observed that the largest RMS values in the AIP occur in the top sector for both basic and optimized intake. However, the optimized intake shows i) a splitter plate trailing edge effect at 0 deg, ii) two clearly separated unsteady pressure zones. Analysis of the RMS contours for all flight conditions revealed that the maximum RMS level in the AIP is reduced by 50% - 84% when changing from basic- to optimized intake duct.

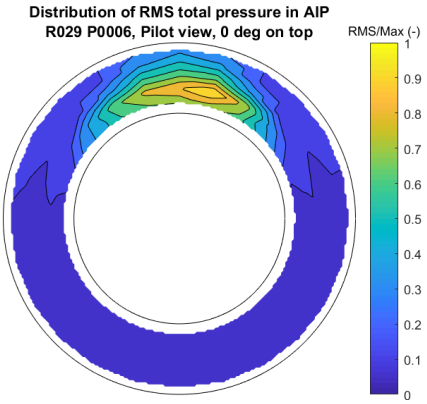

(a) basic

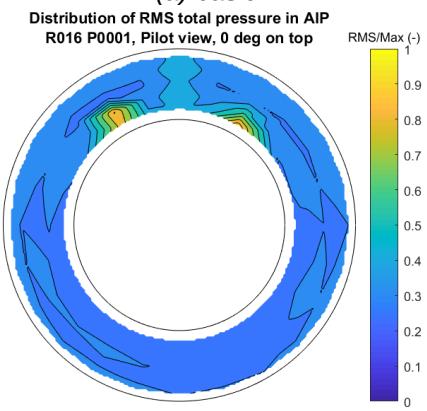

(b) optimized

Fig. 19 Comparison of RMS total pressure distribution in AIP for an AP mode condition

In order to investigate the development of unsteady pressures along the optimized intake duct, 10 sensors have been mounted flush in the intake lip and duct surfaces. Based on the results of the basic intake [14], the optimized intake model design has a different distribution than the basic intake (i.e. focus change from lip, duct symmetry plane and AIP front to lip and side lines in XY-plane, see Fig. 2). Analysis of the RMS static pressure distribution for AP modes revealed that both intake configurations have an overall positive axial gradient in RMS level, where the maxima at the intake “cheeks” are approx. 7% of the mean dynamic head in the AIP for the basic intake, and approx. 3% for the optimized intake.

For VTOL modes a different behaviour is observed. There the basic intake lip also suffers from relative high pressure fluctuations (i.e. approx. 7% suggesting flow separation at lip top and inboard), while the optimized intake lip only has relative high RMS levels of approx. 7% at the inboard zone. The suggestion of flow separation at the optimized duct inboard lip for VTOL is supported by following observations: i) an increased RMS value is also

found at the inboard location as maximum in duct and AIP contour plot, ii) relative low steady total pressure at inboard zone in AIP contour, with shifted $\theta_{max} < 0$ in the $DC60(\theta)$ plot.

5. CONCLUSIONS

A wind tunnel model has been successfully designed and manufactured for full-scale intake testing with modular intake duct configurations. Results of the first test entry, including the basic intake duct, have been reported in an earlier paper [14]. A second wind tunnel test entry with an optimized intake duct has been successfully performed, simulating NGCTR full flight conditions and parameter variations. Evaluation of the test results yields the following trend observations (i.e. optimized- compared to basic intake performance):

- The optimized intake shows significant improvement of the flow quality at the AIP w.r.t. the basic intake. The total pressure based flow distortion descriptors ($DC60MAX$, CDI, $(\Delta P_C/P)_{max}$) show significant reduction for all flight conditions. The radial flow distortion contributions (RDI, $(\Delta P_R/P)_{max}$) are found to be lower than the circumferential ones and in general also show a reduction. For AP and CM modes the averaged reduction in $DC60MAX$ is 74% and for VTOL modes 59% is obtained. The AIP flow topology is characterized by two recirculation areas in the top sector with relative low total pressure. This holds for both basic and optimized intake duct. In addition, the optimized duct contour shows the wake effect of the splitter plate at 0 deg.
- The optimized intake shows a moderate reduction of the velocity based swirl descriptor $SC60MAX$ for all flight conditions, i.e. 9% for AP, 4% for CM and 3% for VTOL.
- The optimized intake shows significant improvement of the total pressure recovery C_{dh} for all flight conditions, i.e. a reduction of 50% for AP, 64% for CM and 41% for VTOL modes.
- It can be observed that in general where the baseline has an adverse pressure gradient in front of the AIP for the bottom line, the optimized intake duct shows an extended flat C_p distribution without any adverse pressure gradient. The basic intake duct top line shows an adverse pressure gradient in the downstream located middle region, while the optimized intake duct top line shows a significantly smaller adverse pressure gradient zone. The optimized duct mitigates the lip suction peak as observed for some conditions (lip bottom line and lip outboard line for some AP modes), however, the strong suction peak at lip top line for VTOL modes persists.
- Both types of intake show an axial development of RMS unsteady static wall pressures along the duct. The optimized intake shows a reduction in the axial gradient of RMS for AP and CM modes. For VTOL modes a different behaviour is observed. The basic intake was found to have the highest RMS level at the “cheeks”, where the lip also suffers from relative high pressure fluctuations (at lip top and inboard a level of 7%, suggesting flow separation). The pressure fluctuations at the lip top location is significantly reduced for the optimized intake (from 7% to 3%), leaving a flow separation effect at the inboard lip. Analysis of the RMS total pressure contours in the AIP for all flight conditions reveals that the maximum RMS level at the AIP is reduced by 50% - 84% when changing from basic- to optimized intake duct.
- A sensitivity analysis has been performed for key flow distortion parameters, in which variation of angle of attack, sideslip, aileron deflection and mass-flow rate has been considered. Both basic- and optimized intake show relative low values for the investigated sensitivities.

6. ACKNOWLEDGEMENTS

This work was performed as part of the project TRINIDAT and has received funding from the Clean Sky 2 Joint Undertaking (JU) under grant agreement No 831810. The JU receives support from the European Union’s Horizon 2020 research and innovation programme and the Clean Sky 2 JU members other than the Union.

This paper reflects only the author’s view; the JU is not responsible for any use made of the information contained herein.

7. REFERENCES

[1] Horizon 2020, Clean Sky 2, Fast Rotorcraft IADP, https://www.cleansky.eu/fast-rotorcraft-iadp

[2] Horizon 2020, Clean Sky 2, TRINIDAT project, GA no. 831810, https://project.nlr.nl/trinidat

[3] SAE-ARP1420 C: Gas Turbine Engine Inlet Flow Distortion Guidelines, Rev. C. April 2017.

[4] G. Gibertini, A. Zanotti, G. Campanardi, F. Auteri, D. Zagaglia, G. Crosta: Wind-tunnel tests of the ERICA tiltrotor optimised air-intake, The Aeronautical Journal, May 2018, Volume 122, No 1251, May 2018.

[5] N. S. Payne: New Large-Scale Model inlet Performance Testing Capability for the AEDC PWT 16 T/S Wind Tunnels, AIAA Aviation Forum, June 25-29, 2018, Atlanta, Georgia, 2018 Aerodynamic Measurement technology and Ground testing Conference.

[6] J. G. Leishman: Principles of helicopter aerodynamics, Cambridge University Press,2000. Section 2.4 Momentum Analysis in Forward Flight.

[7] D.G. MacManus, N. Chiereghin, D. G. Prieto, P. Zachos: Complex Aeroengine Intake Ducts and Dynamic Distortion, AIAA Journal, Vol. 55, No. 7, July 2017.

[8] AGARDograph 109, Subsonic wind tunnel wall corrections, October 1966.

[9] AGARDograph 336, Wind tunnel wall corrections, October 1998.

[10] Labrujère, Th.E., Correction for wall interference by means of a measured-boundary-condition method, NLR TR 84114 U, 1984.

[11] Labrujère, Th.E., Maarsingh, R.A. and Smith, J., Evaluation of measured-boundary-condition methods for 3D subsonic wall interference, NLR TR 88072 U, 1988.

[12] A.C. de Bruin and J. van Muijden, Review of flow field measurement technique with 5-hole rake, NLR-TR-2009-501, NLR, May 2011.

[13] E. Norde, S. van 't Hoff, H. van der Ven, E. van der Weide, F. Spek, Icing characteristics on NGCTR engine inlet for relevant certification conditions, 47th ERF, paper 48, 2021.

[14] R. Habing, I. Philipsen, M. Müller, M. Pecoraro, Experimental evaluation of flow distortion at tilt-rotor full-scale model air intake wind tunnel test, 47th ERF, paper 20, 2021.

[15] B.I. Soemarwoto, R. Habing, M. Pecoraro, Adaptive design method for a tilt-rotor engine inlet duct optimization, AIAA Aviation Forum, DOI: 10.2514/6.2022-4019, 2022.

[16] F. Riccardi et al., NGCTR-TD tilt-rotor autorotation numerical investigation, 78th VFS, paper 1120, 2022.